

Oligomer-based functions of mitochondrial porin

Received: 31 December 2024

Accepted: 8 July 2025

Published online: 25 July 2025

 Check for updates

Hironori Takeda^{1,9,13}, Saori Shinoda^{1,10,13}, Chiho Goto¹, Akihisa Tsutsumi², Haruka Sakaue^{1,3}, Chunming Zhang^{1,3}, Takashi Hirashima^{1,3}, Yuta Konishi¹, Haruka Ono¹, Yu Yamamori^{4,11}, Kentaro Tomii⁴, Hiroya Shiino⁵, Yasushi Tamura⁵, Solène Zuttion⁶, Bruno Senger⁶, Sylvie Friant^{6,12}, Hubert D. Becker⁶, Yuhei Arais⁷, Nanako Kobayashi⁷, Noriyuki Kodera⁸, Masahide Kikkawa² & Toshiya Endo^{1,3} ✉

Porin, or the voltage-dependent anion channel (VDAC), is a primary β -barrel channel in the mitochondrial outer membrane. It transports small metabolites and ions through its β -barrel pore and plays key roles in apoptosis and inflammatory response. Here we report the cryo-electron microscopy structure of yeast porin (Por1) in its hexameric form at 3.2 Å resolution. This structure allows us to introduce various mutations at the protomer interfaces, uncovering three critical functions of Por1 assembly beyond transport. Por1 binds unassembled Tom22, a subunit of the mitochondrial protein import gate (the TOM complex), to facilitate protein import into the intermembrane space, maintains proper mitochondrial lipid composition in the outer membrane through lipid scramblase activity, and contributes to the retention and regulated loss of mitochondrial DNA, in cooperation with nucleases identified through screening enabled by the obtained Por1 mutant.

Mitochondria, chloroplasts, and Gram-negative bacteria are bounded by two membranes, with their outer membranes containing β -barrel membrane proteins that form aqueous pores. Among these, mitochondrial porins, also known as voltage-dependent anion channels (VDACs), play crucial roles in communication and transport across the mitochondrial outer membrane (OM), facilitating the passage of small metabolites and ions¹, regulating Ca^{2+} influx², activating inflammasome³, and participating in the programmed cell death⁴. Porin is composed of 19 β -strands⁵, and its high-resolution structures

in monomeric or dimeric forms have been determined by NMR and X-ray crystallography. These structures were obtained from porins refolded with detergent micelles after denaturation of recombinant proteins expressed in *E. coli* cells^{6–11} or from porins translated in an *E. coli* cell-free system containing detergent/lipid micelles¹². Although porin is thought to form a homo-oligomeric complex¹³, a high-resolution structure of its native assembly is still lacking, hindering a comprehensive understanding of the structure-based mechanisms underlying its physiological functions.

¹Faculty of Life Sciences, Kyoto Sangyo University, Kyoto, Japan. ²Department of Cell Biology and Anatomy, Graduate School of Medicine, The University of Tokyo, Tokyo, Japan. ³Institute for Protein Dynamics, Kyoto Sangyo University, Kyoto, Japan. ⁴Artificial Intelligence Research Center, National Institute of Advanced Industrial Science and Technology (AIST), Tokyo, Japan. ⁵Faculty of Science, Yamagata University, Yamagata, Japan. ⁶Université de Strasbourg, CNRS, Génétique Moléculaire, Génomique, Microbiologie, UMR7156, Strasbourg Cedex, France. ⁷Department of Clinical Laboratory Science, Division of Health Sciences, Graduate School of Medical Sciences, Kanazawa University, Kanazawa, Ishikawa, Japan. ⁸Nano Life Science Institute (WPI-NanoLSI), Kanazawa University, Kanazawa, Ishikawa, Japan. ⁹Present address: Graduate School of Science and Engineering, Saitama University, Saitama, Japan. ¹⁰Present address: Institute for Quantitative Biosciences, The University of Tokyo, Bunkyo-ku, Tokyo, Japan. ¹¹Present address: Center for Computational Sciences, University of Tsukuba, Tsukuba, Ibaraki, Japan. ¹²Present address: INSERM, Université de Strasbourg, UMRS1112, Laboratoire de Génétique Médicale, Centre de Recherche Biomédicale de Strasbourg (CRBS), Strasbourg, France. ¹³These authors contributed equally: Hironori Takeda, Saori Shinoda.

✉ e-mail: tendo@cc.kyoto-su.ac.jp

In this study, we determined the cryo-electron microscopy structure of yeast porin (Por1) in its hexameric form at 3.2 Å resolution. On the basis of this structure, we introduced mutations at the protomer interfaces and revealed Por1 functions beyond metabolite and ion transport, including roles in protein import, lipid scrambling, and mitochondrial DNA maintenance.

Results and discussion

Structure of the porin (VDAC) hexamer

We purified Por1, a yeast porin or VDAC, from solubilized yeast mitochondria (Fig. 1a, b (left)), which showed an apparent molecular weight of ~400–450 kDa on gel-filtration profile (Fig. 1a) and on blue-native (BN)-PAGE gel (Fig. 1b (right)). Its assembly structure was determined by cryo-electron microscopy (cryo-EM) at an effective overall resolution of 3.2 Å (Supplementary Fig. 1a–h and Supplementary Table 1). The mitochondrial porin assembly forms a homo-hexamer with pseudo-2-fold symmetry, comprising two copies of the Por1 trimers, and has approximate dimensions of 170 Å in length, 90 Å in width, and 35 Å in height (Fig. 1c, d). Each porin protomer forms a 19-strand transmembrane (TM) β-barrel structure, with its N-terminal segment (residues 1–13, N-region), penetrating the barrel pore, partially adopting an α-helical structure and interacting with the inner wall of the β-barrel (Fig. 1c, d and Supplementary Fig. 2a). The structure of each protomer closely resembles that of the refolded VDAC monomer^{6–12} (Supplementary Fig. 2b); however, the refolded VDAC does not form a hexamer. The recently reported human VDAC2 dimer, observed in complex with two TOM complex dimers and a PINK1 dimer, has a dimer interface involving β-strands 3–5¹⁴, yet such β-strand interactions were not observed in our Por1 hexamer (Supplementary Fig. 2c, d). When pairs of proximate residues between the Por1 protomers were replaced with Cys pairs and crosslinked by a homobifunctional sulfhydryl-reactive crosslinker, 1,2-ethanedithiol bismethanethiosulfonate (M2M) for intact mitochondria before solubilization with detergent, crosslinked dimers and even a trimer (for the N77C/V217C mutant) were generated, indicating the presence of the Por1 hexamer assembly in intact mitochondria (Fig. 1e). Low-resolution electron microscopy^{15,16} and high-speed atomic force microscopy (HS-AFM)^{17–20} of two-dimensional crystalline arrays prepared from purified mitochondrial outer membranes revealed the architecture of the porin hexamer, which closely resembles the present cryo-EM structure of the Por1 complex (Fig. 1c, d). In addition, HS-AFM observation of the purified yeast Por1 detected particles with oval shapes, consistent with the hexameric assembly determined by cryo-EM, although a height difference was observed between the experimental and simulated topography, likely due to the presence of glyco-diosgenin (GDN) micelles in the experimental data (Supplementary Fig. 1i–k).

Several key interactions can be observed between residues of the porin protomers: for example, T33 and Q194 between protomer pairs of (B, A'), (B', A), (C, B), and (C', B'); R252 and D 228 between protomer pairs of (A, B) and (A', B'); T35 + N37 and S231 + Q249 between protomer pairs of (A', C) and (A', C') (Supplementary Fig. 3a). To assess the roles of the inter-protomer interactions, we imported radioisotope (RI)-labeled Por1 mutants with alterations at these key residue pairs into isolated wild-type (WT) mitochondria in vitro and analyzed their oligomer formation with pre-existing WT Por1 using BN-PAGE, which resolves porin complexes from monomers to hexamers¹³. All the imported Por1 mutants, except Q194A and N37A, were incorporated into the hexameric form less efficiently than the imported WT Por1 (Supplementary Fig. 3b). Por1(Q194A) and Por1(N37A) were incorporated into the hexamer when the remaining five protomers were WT. Notably, these key residues are conserved in human VDAC1 (Supplementary Fig. 2a), suggesting that the hexamer structure is also shared by human VDAC1.

Por1 mutant deficient in Tom22 binding impairs the MIA-pathway protein import

We previously found that the deletion of the yeast *POR1* gene impairs the mitochondrial import of MIA (mitochondrial intermembrane space assembly)-pathway substrates, small Cys-rich soluble proteins in the intermembrane space (IMS), into mitochondria when cultured in a fermentation medium²¹. In intact mitochondria, the TOM complex, which serves as the import gate for most mitochondrial proteins, dynamically alternates between the two forms: the major trimeric complex, which consists of three copies each of Tom40 and Tom22 along with small TOM subunits, and the minor dimeric complex, which contains two copies of Tom40 with small TOM subunits, but lacks Tom22 (Supplementary Fig. 4a). The dimeric form lacking Tom22 specifically functions as the entry gate for MIA-pathway substrates^{21,22}. Since Por1 interacts with free Tom22 molecules that dissociate from the trimeric TOM complex during its conversion to the dimeric TOM complex, the import inhibition of MIA-pathway substrates in *por1Δ* mitochondria likely arose from a substantial failure in the conversion of the trimeric TOM complex to the dimeric complex. However, it cannot be entirely excluded that the observed import inhibition due to Por1 deletion might reflect indirect effects arising from impaired metabolite or ion transport through the Por1 β-barrel pores.

We therefore sought a Por1 mutant that is defective in Tom22 binding but can still transport metabolites and ions as efficiently as WT Por1. Since residue 118 of Tom22, located near the IMS end of the TM helix, is crosslinked to Por1²¹ (Supplementary Fig. 4b), we introduced mutations in pairs of residues involved in Por1 inter-protomer interactions, including the D228-R252 pair (Supplementary Fig. 3a). While the R252E mutation in the D228-R252 pair of Por1 significantly reduced Por1 levels and impaired growth on the respiratory medium, the additional D228K mutation, which restores electrostatic interactions in the D228-R252 pair, rescued both the Por1 level and respiratory growth (Fig. 2a, b). Metabolite (NADH) transport¹ in the D228K/R252E (KE) Por1 mutant strain was comparable to that in the Por1(WT) strain (Fig. 2c). However, the hexamer assembly was destabilized (Supplementary Fig. 4c, d) and crosslinking with residue 118 of Tom22 was absent for Por1(KE) (Fig. 2d). The assembly of newly imported Tom22 into the TOM complex was accelerated in this mutant (Supplementary Fig. 4e), suggesting that Por1(KE) is unable to bind free Tom22 to delay its assembly into the trimer. Consequently, the dimer-trimer exchange was shifted towards the TOM trimer in the Por1(KE) mitochondria, even in the presence of the additional *tom6Δ* mutation (Supplementary Fig. 4c), which typically stabilizes the dimeric form (Supplementary Fig. 4a). Protein levels of the MIA pathway substrates, Tim9, Tim10, and Erv1, were reduced in Por1(KE) as well as *por1Δ* mitochondria, as compared with those in WT mitochondria (Fig. 2e). The in vitro import of MIA-pathway substrates (Fig. 2f), but not TIM23 pathway substrates (Fig. 2g), was impaired in Por1(KE) mitochondria to a similar degree as observed in *por1Δ* mitochondria. These findings suggest that binding of Por1, through interactions involving residues 228 and 252 at its protomer interface, to free Tom22 facilitates the MIA-pathway import by promoting the shift towards the dimeric form of the TOM complex.

Por1 subunit interfaces promote phospholipid scrambling

The structural stability of the Por1 assembly is maintained by both hydrophilic and hydrophobic interactions involving amino acid residues located at the protomer interfaces within the TM β-strands and their flanking segments, in addition to the presence of sandwiched phospholipid molecules; EM densities derived from phospholipid and/or detergent molecules were identified in the spaces between Por1 protomers (Supplementary Fig. 5a). Several hydrophobic residues interact with these phospholipid molecules, acting as a hydrophobic glue that

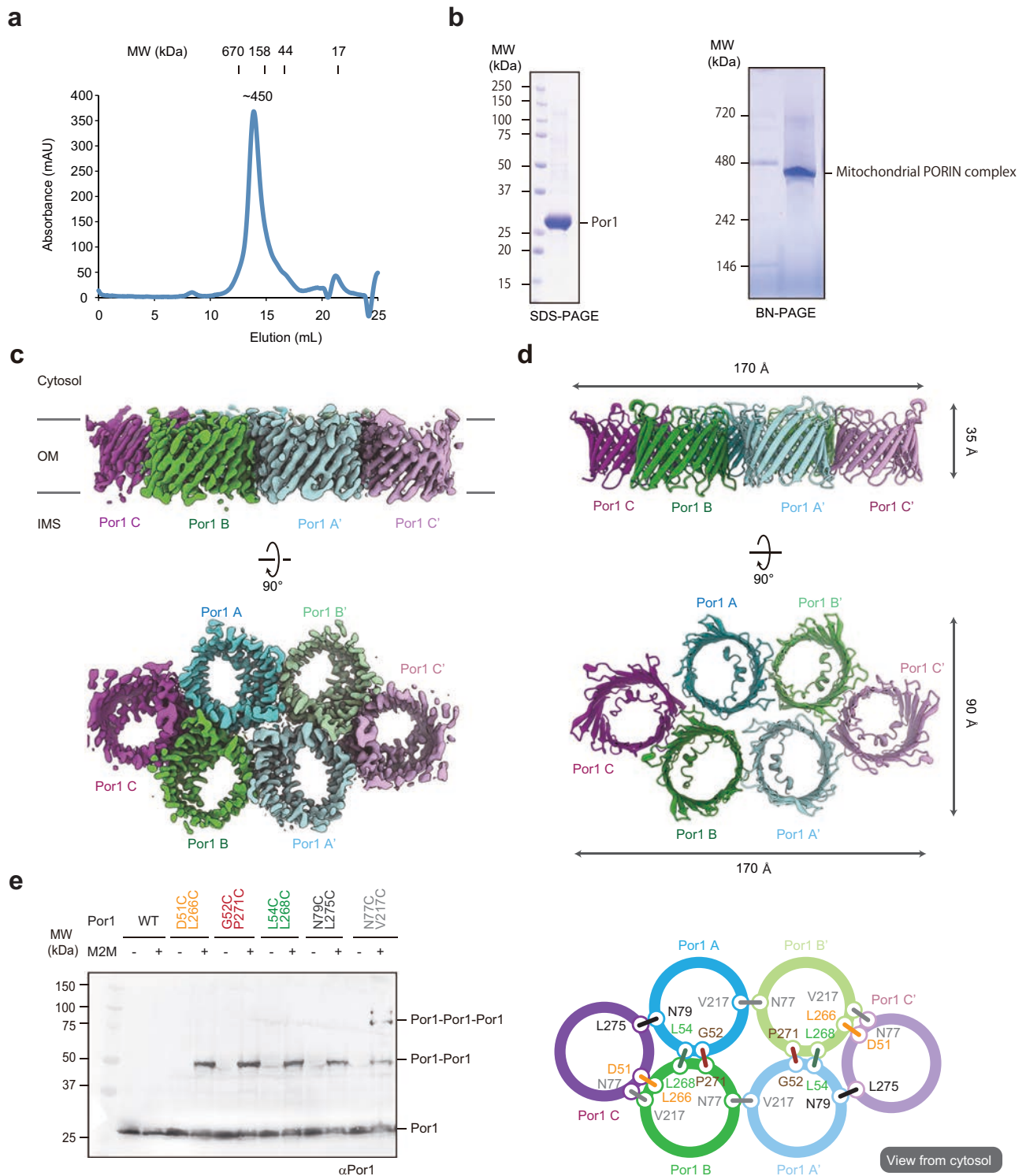


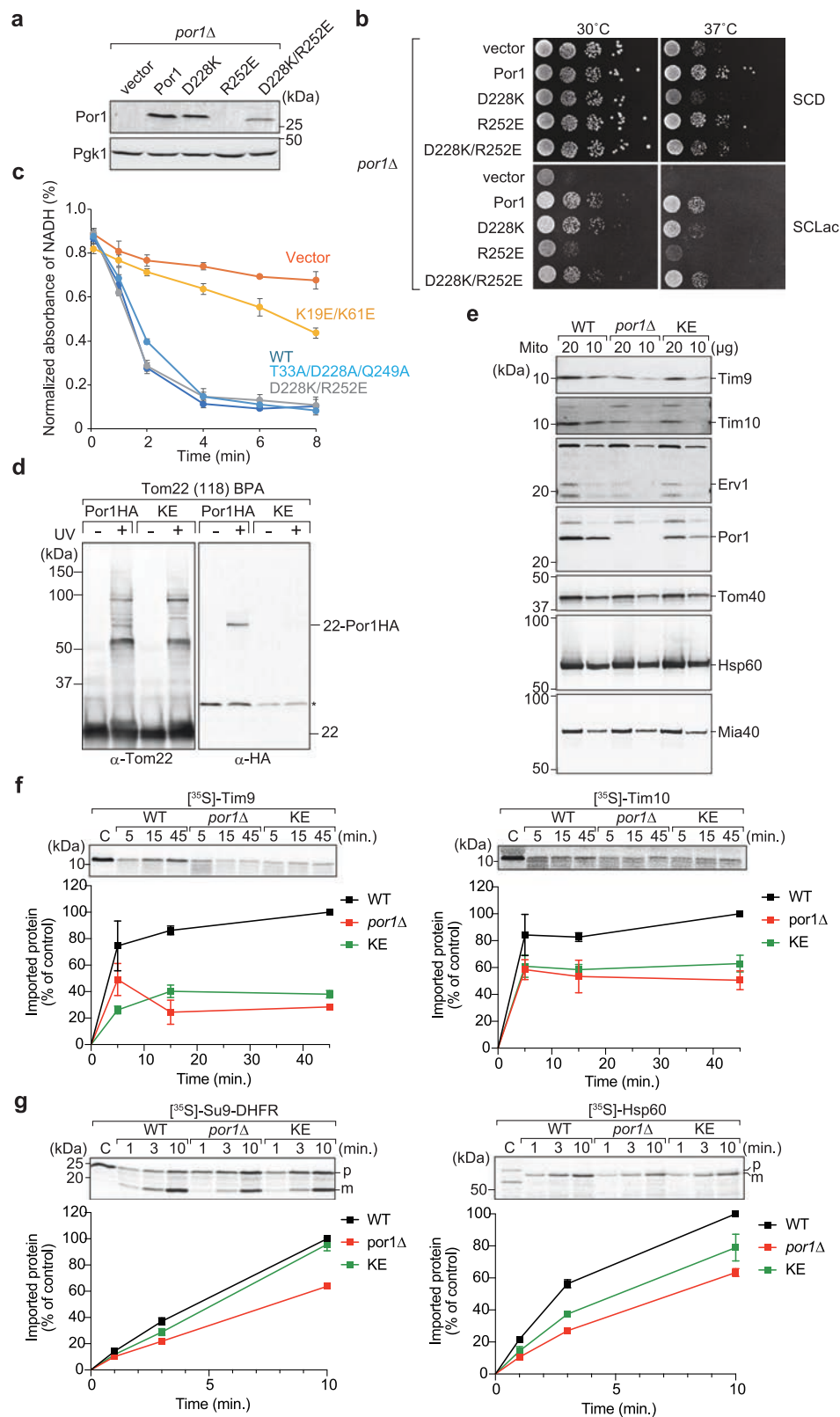
Fig. 1 | Purification and structure of yeast Por1. a Elution profile obtained by gel filtration of the purified Por1 in 0.02% GDN. **b** SDS-PAGE (left) and blue-native PAGE (right) gels of Por1 stained with Coomassie Brilliant Blue (CBB). **c** Cryo-EM density of the Por1 hexamer. **d** Cartoon backbone representation of the Por1 hexamer. **e** Isolated mitochondria with Por1 derivatives containing a pair of Cys residues

(right) were subjected to crosslinking by M2M, and then solubilized and analyzed by SDS-PAGE and immunoblotting with anti-Por1 antibodies. Por1, Por1 monomer; Por1-Por1, crosslinked (Por1)₂ dimer; Por1-Por1-Por1, crosslinked (Por1)₃. Source data are provided as a Source Data file.

stabilizes the hexameric structure of Por1. Such hydrophobic interactions were not observed in the structure of refolded monomeric VDAC⁶⁻¹².

Proper mitochondrial functions rely on the correct lipid composition within mitochondrial membranes, which requires both phospholipid biosynthetic enzymes and lipid transport systems. While

protein mediating lipid transport between the inner membrane (IM) and OM, as well as between the OM and other organelle membranes, have been identified^{23,24}, the mechanism of lipid scrambling – the spontaneous movement of lipids from one leaflet of a membrane bilayer to the other – remains poorly understood. Recently, it was



shown that crosslinked dimers of VDACL1, but not monomeric VDACL1, reconstituted in lipid vesicles, can promote lipid scrambling and that the import of PS across the OM in isolated yeast mitochondria was reduced in mitochondria lacking Por1²⁵. Furthermore, molecular dynamics (MD) simulations have suggested that other oligomeric insertases in the mitochondrial OM may facilitate lipid scrambling²⁶. However, whether the revealed mitochondrial Por1 hexamer indeed

functions as a scramblase in intact mitochondria is still unknown. To address this, we investigated potential lipid transport routes at the subunit interfaces within the determined Por1 hexamer structure.

Coarse-grained (CG) MD simulations were conducted to analyze lipid movement within a hydrated lipid bilayer for the determined Por1 hexamer, alongside Por1 dimers and a Por1 monomer (extracted from the hexamer). The definition of a scrambling event was based on the

Fig. 2 | Por1(KE) mutant is defective in Tom22 binding and impairs the MIA-pathway import. **a** *por1Δ* cells expressing Por1 and mutant Por1 with the indicated mutations, or without expression (vector), were grown in SCD for at 30 °C. Cell extracts were prepared, and proteins were analyzed by SDS-PAGE and immunoblotting with the indicated antibodies. Pgl1, yeast phosphoglycerate kinase 1. **b** Serial dilutions of the *por1Δ* cells expressing Por1 and Por1 with the indicated mutations, or without expression (vector), were spotted on SCD and SCLac media and grown for 2 (SCD) or 3 (SCLac) days at 30 °C and 37 °C. **c** In this NADH transport assay, oxidation of externally added NADH was measured for the indicated reaction times for the indicated mitochondria (*por1Δ* cells expressing Por1 (WT) and mutant Por1 with the indicated mutations, or without expression (vector), which were isolated from cells cultured in YPD. Values are means ± SEMs (*n* = 3). **d** In vivo photocrosslinking of benzoylphenylalanine (BPA) at residue 118 of Tom22 in the indicated strains (*por1Δ* cells expressing WT Por1-HA and Por1(KE)-HA) was

detected by anti-Tom22 antibodies (left) and anti-HA antibodies (right). 22, Tom22; 22-Por1HA, Tom22 crosslinked with Por1-HA. **e** Proteins in mitochondria isolated from the indicated strains were analyzed with the indicated antibodies. **f, g** The indicated mitochondria (WT, *por1Δ*, and *por1Δ* expressing Por1(KE)), isolated from cells grown in YPD, were incubated with the indicated radiolabeled precursors for the indicated times at 25 °C. Tim9 and Tim10 are IMS-localized MIA-pathway substrates, and Su9-DHFR and Hsp60 are matrix-localized TIM23-pathway substrates. Then the mitochondria were treated with 50 μg/mL proteinase K for 15 min on ice (for Su9-DHFR and Hsp60) or diluted 10-fold with ice-cold buffer containing 50 mM iodoacetamide and 50 μg/mL proteinase K for 15 min on ice (for Tim9 and Tim10), and PMSF was added to 1 mM. The proteins were analyzed by SDS-PAGE and radioimaging; quantification was plotted against time (bottom), where the maximum amount for WT mitochondria was set to 100%. Values are means ± SEMs (*n* = 3). C, 10% of the input. Source data are provided as a Source Data file.

orientation of a lipid molecule relative to the membrane's perpendicular axis, following the criteria outlined in a recent study²⁶. Lipid scrambling was observed for the Por1 hexamer with higher efficiency compared to the Por1 dimers (Supplementary Movie 1). In contrast, only marginal scrambling was observed for the Por1 monomer and no scrambling happened in the pure hydrated lipid bilayer (Supplementary Fig. 5b). The VDAC dimer interface (β 1, β 2, β 8, and β 19), previously proposed to facilitate lipid scrambling²⁵, is located within the confined space in the Por1 hexamer (Supplementary Fig. 5c). This spatial restriction makes it unlikely that this interface plays a direct role in mediating lipid scrambling, unless the Por1 or VDAC hexamer undergoes dynamic assembly and disassembly that permits lateral lipid diffusion into and out of the confined space. Mapping the positions of scrambling events onto the Por1 hexamer structure on the membrane's horizontal plane revealed that most scrambling occurred at the interfaces between Por1 protomers (Fig. 3a). However, the scrambling efficiency varied across different protomer interfaces, with the highest efficiency observed at the B/C and B'/C' interfaces, where hydrophilic, mostly conserved, residues are aligned across the OM. In contrast, the A/C and A'/C' interfaces, which exhibited the lowest efficiency, have Q73 in Por1 less accessible, compared to other interfaces. The frequently involved residues at the interfaces are color-coded in Fig. 3b, with hydrophilic or polar residues (R, N, D, E, Q, K, S, T, H, and C) shown in red, and all other residues in gray. Notably, in the B/C interface, there is a prominent alignment of red residues, suggesting the potential formation of a hydrophilic pathway that allows phospholipid head groups to traverse the membrane while their acyl chains remain in the hydrophobic core of the lipid bilayer. This could facilitate lipid scrambling. Alternatively, the aligned polar residues might cause local membrane thinning, reducing the distance for lipid head groups to cross the lipid bilayer. Notably, one of the aligned conserved residues, Q73 in Por1, is replaced by E73 in human VDAC (Supplementary Fig. 2a). The effects of this change were investigated through all-atom MD simulations for VDAC1²⁷. Interestingly, in Por1, the Q73E mutation enhances scramblase activity for both oligomers and dimers, particularly in the hexamer, while the Q73V replacement suppresses scrambling activity (Supplementary Fig. 5b). These findings suggest that the role of VDAC in lipid scrambling in human mitochondria may be more significant than that of Por1 in yeast mitochondria.

To assess the suggested role of lipid scrambling in the Por1 hexamer, we introduced three Ala substitutions at key subunit interaction sites (T33A/D228A/Q249A, referred to as the TDQ mutant, Supplementary Fig. 6a) and analyzed the phospholipid composition in TDQ mutant cells. The TDQ mutation did not affect Por1 expression levels or cell growth, yet it did impair the hexamer assembly (Supplementary Fig. 6b–d). It is to be noted that the metabolite (NADH) transport was not affected in TDQ mutant mitochondria compared to WT Por1 mitochondria (Fig. 2c). Our results showed that the TDQ Por1 mutant exhibited reduced levels of cardiolipin (CL), suggesting the disturbed

phospholipid transport in TDQ mutant mitochondria (Fig. 3c). Although PE is also synthesized in mitochondria like CL, the amount of PE remained unchanged in the TDQ Por1 mutant. This is likely because PE is synthesized not only by the mitochondrial enzyme Psd1 but also by the extramitochondrial PE synthase Psd2 and the Kennedy pathway at the ER²⁴. These additional sources may mask subtle changes in PE levels, unlike CL, which is synthesized exclusively within mitochondria. These findings support the idea that the hexameric structure of Por1 is important for its lipid scramblase activity, although the precise relationship between hexamer stability and scramblase function still remains to be elucidated.

Por1 plays a key role in maintaining mtDNA integrity

In human mitochondria, the release of mtDNA to the cytosol, which has similarities to bacterial DNA with unmethylated CpG motifs^{25–32}, triggers an inflammatory response^{33,34}. Yeast cells also lose mtDNA to become respiratory-deficient ρ^0 mutants. Translocation of fragmented mtDNA to the nucleus has been observed in both humans and yeast and is implicated in various biological processes and diseases, including aging^{35,36}. Although the mechanism of mtDNA release remains largely unknown, VDAC in human mitochondria was suggested to release mtDNA fragments through pores formed by higher-order VDAC oligomers under moderate stress conditions^{33,37}. Of Por1 mutants with substitutions in residues at the protomer interface (Supplementary Fig. 3a), we identified an Ala mutant at residue 194 (Q194) in the hydrophilic 33–194 pair at the protomer interface (Q194A), which generated small white colonies on fermentation medium, indicative of a respiratory-deficient phenotype, at a significant frequency. This mutant also exhibited defective growth on respiratory medium (Fig. 4a). SYBR Green staining revealed that, while WT and *por1Δ* cells showed mtDNA signals colocalized with mitochondrial markers, the Q194A (QA) mutant lacked such signals and displayed mitochondria with altered morphology, suggesting a loss of mtDNA (Fig. 4b). Furthermore, qPCR analysis showed that the Por1(QA) mutant, out of 12 different *por1* mutant strains, lost the *COX2* gene from its mtDNA (Fig. 4c). Since conserved Q194 is replaced with His in some fungal species and plants (Supplementary Fig. 2a), we asked if the Q194H replacement would affect mtDNA levels but found that it did not (Fig. 4d). We further confirmed through qPCR that the Por1(QA) mutant also led to the loss of another mtDNA locus, the 15S rRNA gene (Fig. 4e). While the QA mutation did not significantly impact Por1 expression levels, it caused a shift of Por1 to a larger assembly or aggregated form (Supplementary Fig. 7a, b).

What is the mechanism behind the loss of mtDNA by the Por1(QA) mutant? A simple yet plausible explanation is the inhibition of mtDNA replication, followed by the dilution of mtDNA copies per cell as the cells proliferate. To address this possibility, we followed the time course of the mtDNA levels using qPCR in Por1(QA) cells, which were first grown in respiration (galactose) medium, forcing them to retain

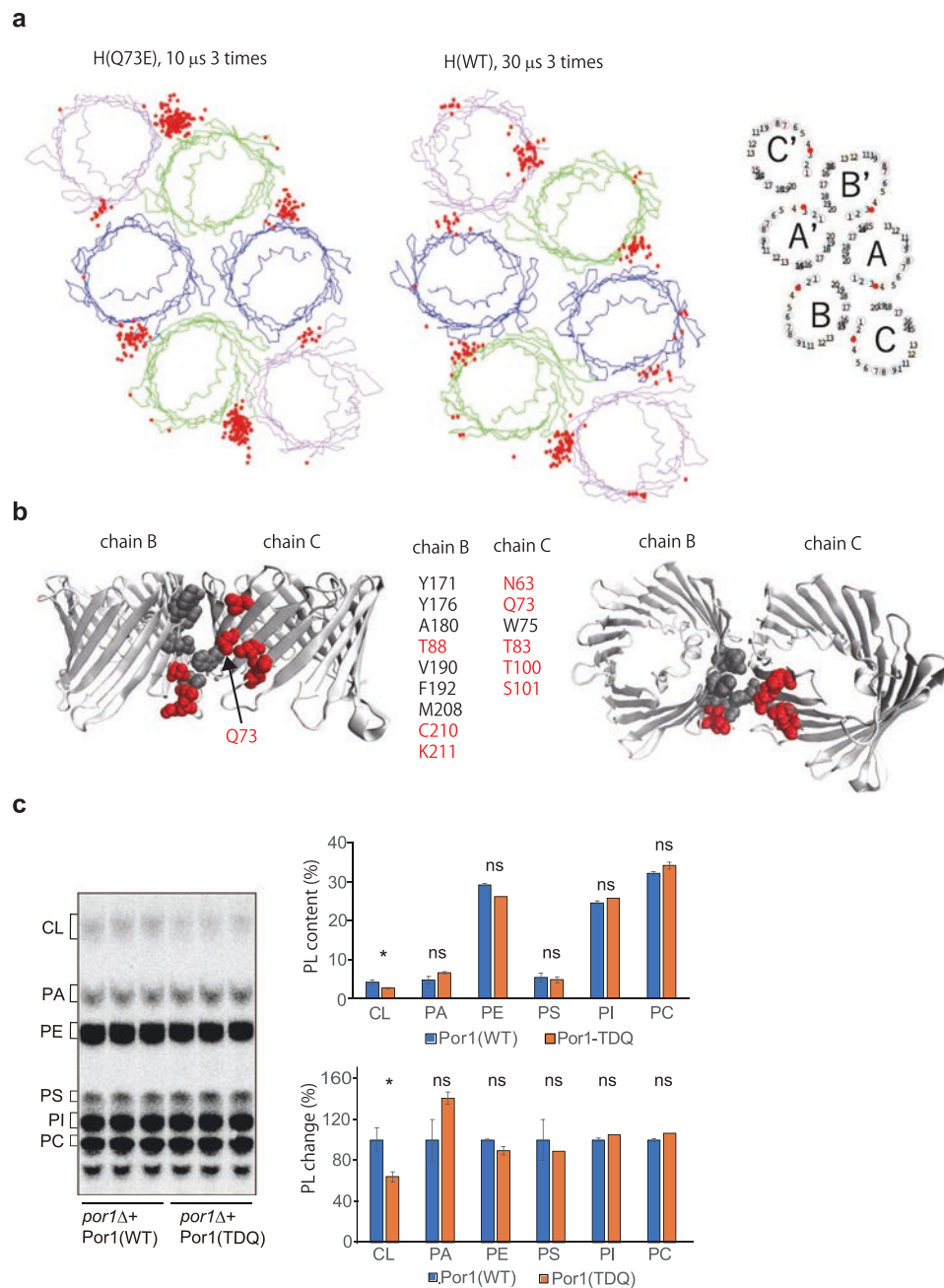


Fig. 3 | Por1 hexamer has a phospholipid scramblase activity. **a** CGMD simulation of Por1(QE) and WT Por1 hexamers were conducted. Three independent simulations were run for 10 μ s for Por1(QE) and 30 μ s for WT Por1. The protein structures and their initial positions are those at the start of the simulation. Red dots indicate the positions of the phospholipid head groups (PO_4) that underwent scrambling, indicating that scrambling is more likely to occur at the B-C and B'-C' interfaces. **b** Each atom of the residues frequently involved in scrambling at the B/C interface is represented by a sphere in both the side view (left) and top view (right), and the corresponding residues are listed (center). Hydrophilic or polar residues

are highlighted in red. **c** Total phospholipids were extracted from the indicated cells grown in YPD containing [32 P]-Pi and analyzed by thin-layer chromatography and radioimaging (Left). CL, cardiolipin; PA, phosphatidic acid; PE, phosphatidylethanolamine; PS, phosphatidylserine; PI, phosphatidylinositol; PC, phosphatidylcholine. The relative amounts of each phospholipid are shown as a percentage of total phospholipids (Top Right) and compared to those in WT control cells (Bottom Right). Values are means \pm SEMs ($n = 3$). *ns*, not significant. $^*p \leq 0.046$, p -values were obtained from the unpaired two-tailed t test. P -value for CL is 0.046. Source data are provided as a Source Data file.

mtDNA for survival, and then switched to glucose medium (Supplementary Fig. 7c). In Por1(QA) cells, the mtDNA level dropped rapidly to 30% within 3 h, then to 20% after another 3 h, where it leveled off. In contrast, WT cells and *por1* Δ cells complemented with Por1 showed a more gradual decrease, with mtDNA levels decreasing to 60–80% in 3 h and 50% in 6 h, but recovering quickly due to the diauxic shift in their metabolism³⁸. Given that the doubling time of these cells was approximately 1.9 h under these conditions (data not shown), the rapid

decline in mtDNA levels in Por1(QA) cells cannot be solely attributed to impaired mtDNA replication. In human mitochondria, VDAC-dependent mtDNA loss has been shown to require the mitochondrial nuclease ENDOG and the presence of positively charged residues in the N-terminal segment preceding the β -barrel domain of VDAC, which serve as binding sites for negatively charged mtDNA, facilitating its escape to the cytosol³⁷. We thus tested the effects of depleting the yeast ENDOG homolog Nucl (*nuc1* Δ) and replacing three positively charged

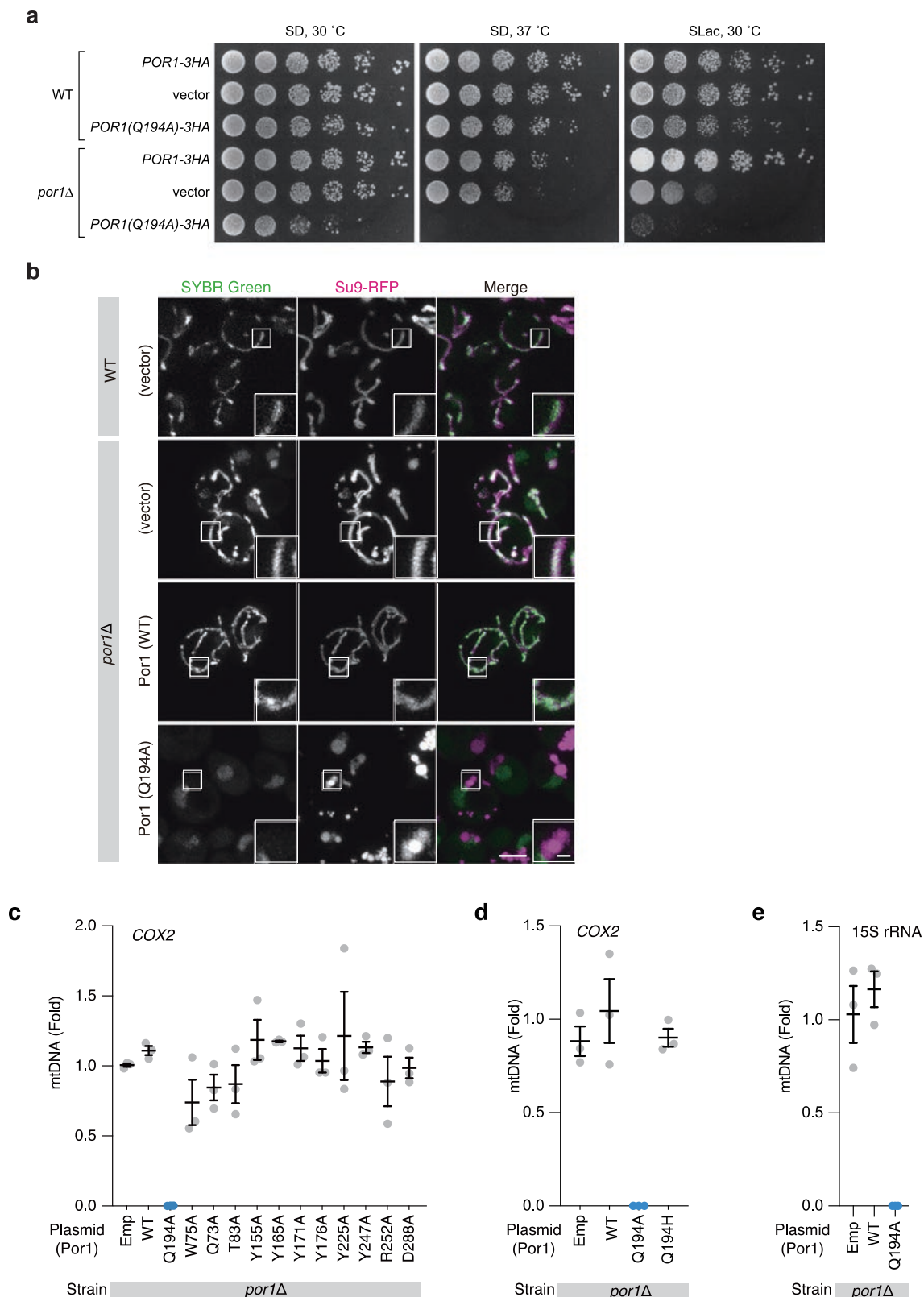


Fig. 4 | The Por1(Q194A) mutant causes mtDNA loss. a Serial dilutions of the WT and *por1*Δ cells expressing Por1-HA and Por1(QA)-HA, or without expression (vector), were spotted on SD and SLac media and grown for 2 (SD) or 6 (SLac) days at 30 °C and 37 °C. **b** WT and *por1*Δ cells expressing Por1 and Por1(QA), or without expression (vector), together with the expression of Su9-RFP, were incubated with SYBR Green for mtDNA labeling in SCD media at 30 °C for 4 h and imaged by confocal microscopy. Scale bars: 5 μm (main images), 1 μm (inset).

c–e Quantification of mtDNA in *por1*Δ cells expressing the indicated Por1 mutants from its own promoter via plasmid transformation. The amount of mtDNA was calculated based on the Cq value of the mtDNA-encoded *COX2* (**c, d**) or 15S rRNA (**e**) gene, normalized to the nuclear-encoded *ACT1* gene. The Y-axis represents mtDNA (Fold) normalized to the W303-1A WT cells. Values are means ± SEMs ($n = 3$). Source data are provided as a Source Data file.

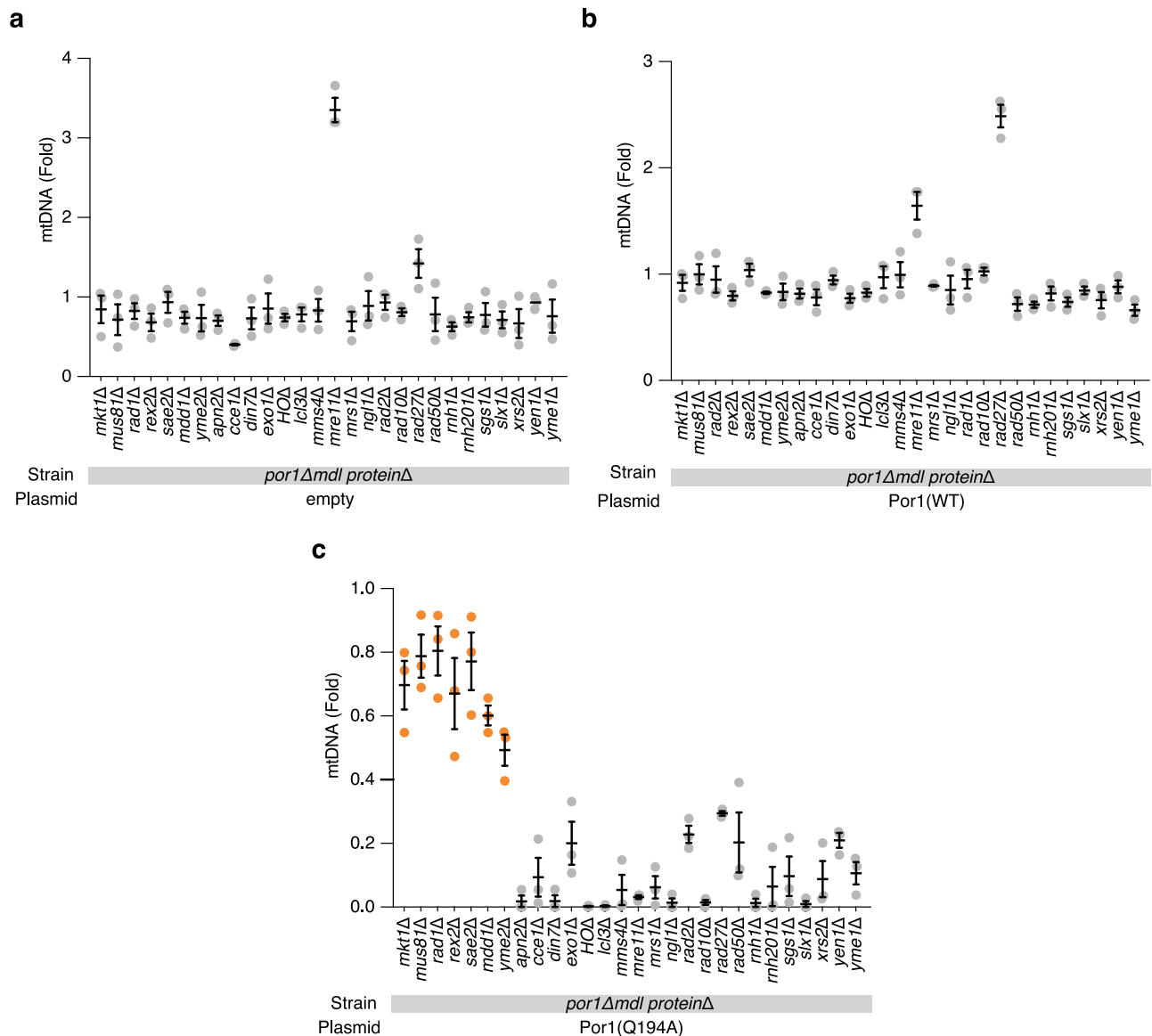


Fig. 5 | Identification of MDL proteins involved in the mtDNA loss by Por1(QA). a–c Quantification of mtDNA in the double deletion mutants of *POR1* and indicated genes without expression (a) or with expression of WT Por1 (b) and Por1(QA) (c)

from its own promoter via plasmid transformation. The amount of mtDNA was calculated as in Fig. 4c. Values are means \pm SEMs ($n = 3$). Source data are provided as a Source Data file.

residues at positions 11, 19, and 23 in the N-terminal segment with neutral Ala residues (Por1-N3A). However, neither mutation suppressed mtDNA loss in Por1(QA) cells (Supplementary Fig. 7d). We also confirmed that deletion of *ATG1*, the most upstream gene in the autophagy pathway³⁹, did not prevent mtDNA loss in Por1(QA) cells, indicating that autophagy is not involved (Supplementary Fig. 7d). Since mitochondrial transcription factor A (TFAM) is implicated in the loss of mtDNA^{40,41}, we tracked the localization of fluorescent protein-tagged Abf2, a yeast homolog of TFAM. In Por1(QA) cells, the Abf2 derivative was observed not only within the mitochondrial interior but also at the mitochondrial periphery, which is in contrast to its localization within the mitochondrial interior in WT cells (Supplementary Fig. 7e).

These results suggest that the Por1(QA) mutant provides a useful tool for identifying factors involved in mtDNA loss, including mtDNA escape and/or degradation, in yeast cells. To screen for nucleases responsible for mtDNA loss in the Por1(QA) mutant, we made deletion mutants for 26 potential yeast nucleases and nuclease-related proteins, as well as Yme2, which was reported to be involved in the transfer of

mtDNA fragments to the nucleus⁴², in the QA mutant background. We found that deletion of seven genes – *MKT1*, *MUS81*, *RADI*, *REX2*, *SAE2*, *MDD1* (YBL055C, named *Mitochondrial DNA Degradation 1*), and *YME2* – stabilized mtDNA in the Por1(QA) strain but not in the strain with Por1(WT) or without Por1 (Fig. 5a–c and Supplementary Fig. 8a), and termed them mtDNA-losing (MDL) proteins. Other deletion strains either did not stabilize mtDNA or did so only marginally in the Por1(QA) background. Sae2, whose depletion stabilized mtDNA in the Por1(QA) strain, is a subunit of the MRX complex, which is involved in the repair of chromosomal DNA double-strand breaks in the nucleus⁴³. However, depletion of the other three subunits of the MRX complex – Xrs2, Rad50, and Mre11 – did not stabilize mtDNA or did so only partially in the Por1(QA) cells (Fig. 5a–c and Supplementary Fig. 8a). Depletion of Mre11 of the MRX complex, as well as depletion of Cce1 and Rad27, affected the mtDNA levels even in cells lacking Por1 and/or containing Por1(WT) (Fig. 5a–c and Supplementary Fig. 8a).

What is the mechanism by which depletion of the seven MDL proteins suppresses Por1(QA)-mediated mtDNA loss? To address this,

we analyzed the cellular localization of these MDL proteins using two independent approaches: microscopic observation of their fluorescent protein derivatives, and specific detection of the mitochondrial ‘echoforms’ of these proteins by observation of GFP signals from split-GFP fragments – one expressed inside the mitochondria from the mtDNA and the other fused to the protein of interest⁴⁴. Among the seven MDL proteins identified as stabilizing mtDNA in the Por1(QA) mutant, Mkt1, Rad1, Rex2, Mdd1, and Yme2 were localized to mitochondria (Supplementary Fig. 8). In contrast, Sae2 and Mus81 were predominantly localized in the cytosol and nucleus (Supplementary Fig. 8). Yme2, a single-pass IM protein, has its N-terminal part colocalized with mitochondrial nucleoids⁴⁵, interacts with the soluble DNA exonuclease Rex2 in the matrix^{46,47}, and its C-terminal part, containing an AAA+ domain, likely oligomerizes in the IMS⁴², yet its GFP signal arising from its association with the matrix-localized GFP fragment was observed. Indeed, IMS-localized domains, in addition to matrix-localized proteins, were previously detected by localization analysis using split GFP fragments⁴⁸.

Next, we analyzed mtDNA localization in deletion mutants of the seven MDL protein-encoding genes, all in the background of the Por1(WT) or Por1(QA) mutation (Fig. 6a, b). SYBR Green staining revealed that, in all seven deletion mutants with the Por1(QA) mutation, presumably partially degraded mtDNA appeared to be localized around the mitochondria (Fig. 6b (left)). As controls, mtDNA stays in mitochondria in these MDL-protein deletion mutants with Por1(WT) (Supplementary Fig. 9). Plot profiles further indicated that in some of the MDL-protein deletion mutants, such as *mdd1Δ*, *mus81Δ*, *sae2Δ*, and *yme2Δ*, mtDNA was positioned at the periphery (either in the IMS or on the mitochondrial surface) rather than within the mitochondrial interior (Fig. 6b (right)). These findings suggest that, in the Por1(QA) strain, mtDNA is likely fragmented within the mitochondria, which may facilitate the translocation of mtDNA fragments across the IM and the OM (Fig. 6c). Once in the cytosol, these fragments would likely be degraded by different nucleases. In the Por1(WT) strain, the MDL nucleases appear to be inactive or enzymatically latent within mitochondria, but they may become active or accessible in the Por1(QA) mutant through an unknown signal transduction from Por1(QA) in the OM to the mitochondrial interior. The role of alteration of the Por1 assembly structure by the QA mutation in such a signal transduction remains unclear.

In conclusion, Por1 prevents the leakage of mtDNA to the cytosol, thereby protecting it from degradation. This suggests a potential role for porin in the regulated loss of mtDNA, possibly in cooperation with MDL proteins under specific conditions. The functions of Por1 revealed in this study, namely its involvement in protein import and lipid scrambling, and in particular, mtDNA maintenance, beyond its established role in transporting small metabolites and ions through its β -barrel pore, are likely associated with its interactions with various proteins, positioning Por1 as a key hub in mitochondrial functional networks.

Methods

No statistical methods were used to predetermine sample size. The experiments were not randomized, and investigations were not blinded to allocation during experiments and outcome assessment.

Yeast strains, plasmids and primers

The yeast strains, plasmids, and primers used in this study are listed in Supplementary Tables 2–4. To construct the *Saccharomyces cerevisiae* strain for Por1 overexpression, a DNA fragment for the *CgTRP1-GALI* cassette was amplified by PCR and inserted into the 5' region of the *POR1* locus. For affinity purification of Por1, a DNA fragment for hphMX6-His₆ was inserted. To construct yeast strains for the crosslinking and hexamer mutant assays, a DNA fragment containing the promoter and protein-coding region of *POR1* was amplified by PCR and inserted into the pRS314 plasmid, which carries the *TRP1* cassette. Subsequently, point

mutations were introduced into the *POR1* gene by PCR, and the resultant plasmids were transformed into the *por1Δ* strain²¹.

Yeast strains for gene deletion and protein tagging were constructed by PCR-mediated homologous recombination⁴⁹ and verified by PCR genotyping followed by sequencing. To generate the *por1Δ* strain, the open reading frame of *POR1* was replaced with *Candida glabrata HIS3(CgHIS3)*²¹. The *por1Δ* strain was transformed with pRS316-*ownp*-Por1 mutant plasmids (Supplementary Table 3). For AFM analysis, Por1-His₁₂ was expressed from the *Z4EV* promoter at the *LEU2* locus, while the transcriptional factor *Z4EV* was expressed from the *ADHI* promoter at the *TRP1* locus of the *por1Δ* strains. For endonuclease screening, the open reading frame of each gene was replaced with *KanMX4* in the *por1Δ* strains. For fluorescence microscopy, endonucleases (and related proteins) and Abf2 were tagged with mNeonGreen at their C-termini and expressed from their own promoters. For nuclease (and related protein) overexpression, the WT strain was transformed with pRS316-GPdp-nuclease (or related protein)-mNeonGreen plasmids (Supplementary Table 3). These strains also expressed Su9-RFP as a mitochondrial marker, integrated into the *HIS3* locus under the control of the *ADHI* promoter.

To construct the RKY176 *S. cerevisiae* Bi-Genomic Mitochondrial-Split-GFP strain (Supplementary Table 1), the first ten β -strands of GFP (GFP _{β 1-10}) were encoded in the mitochondrial genome⁴³. This strain was then transformed using the PEG-LiAc method with pRS414-GPdp-nucleases- β II_Cyct plasmids (Supplementary Table 3), enabling the expression of proteins C-terminally tagged with GFP _{β 11}.

Protein expression and purification

For cryo-EM structural analysis, the Por1 complex was purified from *S. cerevisiae* strain W303a, which expresses Por1 with a C-terminal His₆ tag from the *GALI* promoter. After culturing in 20 L of SCD (-Trp) medium at 30 °C for 24 h, 2% galactose was added to the medium, and incubated at 30 °C for an additional 12 h. The yeast cells were resuspended in DTT (dithiothreitol) buffer (50 mM Tris-HCl, pH 9.4, 10 mM DTT) and incubated at 30 °C for 1 h. To remove the cell wall, the cells were collected, resuspend in Zymolyase buffer (50 mM KPi, pH 7.2, 1.2 M sorbitol, 5 mg zymolyase per 1 g of cells), and incubated at 30 °C with shaking for 5 h. The resultant spheroplasts were collected, resuspended in breaking buffer (50 mM Tris-HCl, pH 8.0, 0.6 M sorbitol, 1 mM EDTA, 0.1 mM PMSF), and disrupted using 200 strokes of a Dounce homogenizer. The homogenate was centrifuged at 1500 \times g for 10 min at 4 °C to remove debris. The supernatant was then centrifuged at 15,000 \times g for 30 min at 4 °C, and the resultant pellet was washed with SEM (50 mM MOPS-KOH, pH 7.2, 1 mM EDTA, 0.6 M sucrose). Mitochondria were isolated by centrifugation at 15,000 \times g for 30 min, 4 °C, and lysed in 200 mL solubilization buffer (50 mM Tris, pH 8.0, 150 mM NaCl, 5 mM DTT, 1% digitonin) at 4 °C for 1 h. The solubilized mitochondria were incubated with Ni-NTA affinity resin (pre-equilibrated with solubilization buffer containing 0.1% digitonin (Merck, #300410)) for 30 min. The resin was washed with solubilization buffer containing 0.1% digitonin and 25 mM imidazole, and the mitochondrial Por1 complex was eluted with solubilization buffer containing 0.1% digitonin and 250 mM imidazole. The eluted fraction was subjected to gel filtration using a Superose 6 10/300 GL column (GE Healthcare, 29091596) equilibrated with gel-filtration buffer (25 mM Tris-HCl, pH 7.5, 150 mM NaCl, 2.5 mM DTT, 0.02% glycodiosgenin (GDN; Anatrace, #GDN101)). The purified mitochondrial Por1 complex was concentrated to 6 mg/mL with an Amicon Ultra-0.5 filter (Merck Millipore, 100 kDa MW cut-off).

Yeast growth conditions

Yeast strains were cultured in YP (1% yeast extract, 2% glucose, and 2% polypeptone), SCD (0.67% yeast nitrogen base without amino acids, 0.5% casamino acids, 2% glucose), SCGal (0.67% yeast nitrogen base

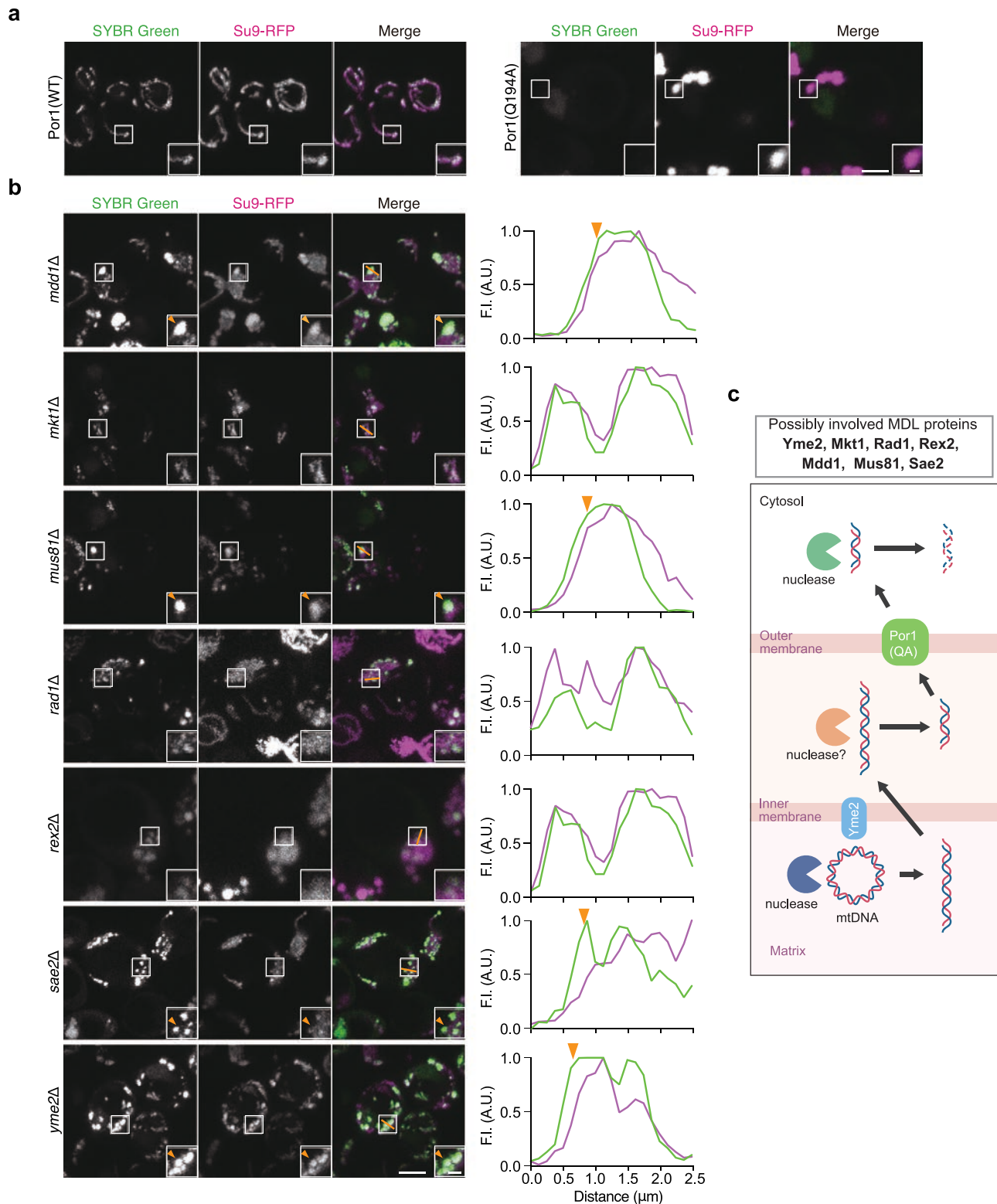


Fig. 6 | mtDNA is localized in mitochondria in the Por1 (QA) strains lacking the MDL proteins. a, b Cells lacking Por1 (a) and those lacking Por1 and one of the MDL proteins (b) but expressing Por1(WT) (a, left) or Por1(QA) (a, right; b) from their own promoters via plasmid transformation, were incubated with SYBR Green for mtDNA labeling in SCD medium at 30 °C for 4 h. Z-max projection images are shown. The boxed regions are magnified. Experiments were performed independently three times. Scale bars: 5 μ m (main images), 1 μ m (inset). Fluorescence

intensity (F.I. (arbitrary unit)) profile of mtDNA (green) and Su9-RFP (magenta) along the orange lines in the left panels are shown in the right panels. Orange arrowheads indicate mtDNA-positive and Su9-negative signals. c A proposed model for the mtDNA loss caused by Por1(QA). The roles of Por1(QA) and Yme2 in mtDNA escape from mitochondria are not clear. Source data are provided as a Source Data file.

without amino acids, 0.5% casamino acids, 2% galactose), SCLac (0.67% yeast nitrogen base without amino acids, 0.5% casamino acids, 2% sodium lactate), SD (0.67% yeast nitrogen base without amino acids, 2% glucose), and SLac (0.67% yeast nitrogen base without amino acids, 2% sodium lactate) media.

Cryo-EM grid preparation

The concentrated mitochondrial Por1 complex in GDN micelles was applied onto a Quantifoil holey carbon grid (R1.2/1.3 Au, 300 mesh) after a 30 s glow discharge. The grid was blotted for 6 s under 100% humidity at 6 °C, and then plunge-frozen in liquid ethane using a Vitrobot Mark IV (Thermo Fisher Scientific).

Cryo-EM data acquisition and image processing

Cryo-EM data were acquired using a Titan Krios G3i cryo-electron microscope (Thermo Fisher Scientific) at the University of Tokyo, operating at 300 kV under low-dose conditions. A total of 4876 micrographs were collected on a Gatan K3 Summit direct electron detector in electron counting mode, with an energy filter set to 25 eV. Forty movie frames were recorded for each micrograph, with an exposure of 1.0 e⁻/Å² per frame. Imaging was performed at a nominal magnification of 105,000 \times , corresponding to a calibrated pixel size of 0.83 Å.

The movie frames were motion-corrected using MotionCorr in RELION⁵⁰, and contrast transfer function (CTF) parameters were estimated using CTFFIND4⁵¹. Micrographs with a CTF resolution better than 6 Å were selected, yielding 4876 usable micrographs. To generate templates for 2D reference-based particle picking, particles were first selected from 100 randomly chosen micrographs using a 3D reference-based method with an initial 3D model of Por1 obtained from previous experiments. The best 2D classes were then used as templates for picking particles across all 4876 micrographs, resulting in the identification of 1,477,608 particles. These particles were down-sampled to a pixel size of 3.63125 Å/pix and subjected to one round of 2D classification and two rounds of 3D classification, yielding 78,760 particles. The selected particles were re-extracted at a pixel size of 1.245 Å/pix and used for 3D refinement. All 3D refinements were performed with C2 symmetry. Following CTF refinement, Bayesian polishing, and a second round of CTF refinement, the final 3D refinement and post-processing resulted in a 3.2 Å resolution 3D map of the Por1 hexamer structure, determined according to the FSC = 0.143 criterion⁵² (Supplementary Table 1).

Model building and refinement

An initial model for the mitochondrial Por1 complex was obtained by fitting the structure of human VDAC1 (PDB ID:3EMN) into the cryo-EM density map using UCSF Chimera⁵³. The atomic model for all protomers of the mitochondrial Por1 complex was then built de novo into the EM density map using COOT⁵⁴ and subsequently refined with Phenix⁵⁵. Molecular graphics were illustrated with CueMol⁵⁶.

HS-AFM observation

HS-AFM analysis was performed in solution at room temperature using a laboratory-built HS-AFM setup^{57,58}. The general procedure for HS-AFM observation of protein molecules is described elsewhere⁵⁹, but in brief, a glass sample stage (2 mm in diameter, 2 mm in height) with a thin mica disc (1.5 mm in diameter, 0.05 mm thick) glued to the top with epoxy was mounted onto the Z-scanner using a drop of nail polish. The mica surface was treated with (3-aminopropyl)triethoxysilane (APTES) to promote the grounding of Por1 particles. A 2 μ l drop of solubilized Por1 complex was deposited onto the mica surface. Purified Por1 was taken from the peak fraction of the gel filtration chromatogram and diluted with a buffer containing 25 mM Tris-HCl, pH 7.5, 150 mM NaCl, 2.5 mM DTT, and 0.02% GDN for better dispersion. After 5 min of incubation, the sample stage was immersed in a liquid cell

containing -60 μ l of the same buffer. HS-AFM imaging was performed in a tapping mode using small cantilevers (BLAC10DS-A2, Olympus) with a resonant frequency of -0.5 MHz and a quality factor of -1.5 in water, and a spring constant of -0.1 N/m. The probe tip was extended from the original cantilever tip by electron beam deposition using ferrocene, followed by sharpening with a radio-frequency plasma etcher (Tergeo, PIE Scientific LLC) under an argon gas atmosphere (Direct mode, 10 sccm, 20 W for 1.5 min). Imaging conditions were either 1.3 frames per second with a scan size of 250 \times 250 nm² and a pixel resolution of 270 \times 63, or 6.6 frames per second with a scan size of 80 \times 56 nm² and a pixel resolution of 300 \times 70. Simulated AFM images were generated by the Biomolecular AFM viewer⁶⁰ with a probe curvature radius of 10 nm, a cone angle of 10 degrees, and a pixel size of 1 nm.

In vitro import, BN-PAGE analysis, and crosslinking analysis

In vitro mitochondrial protein import and BN-PAGE analysis²¹ were performed as follows. Briefly, pGEM4z vectors carrying ORFs of mitochondrial precursor proteins were used for in vitro transcription with SP6 RNA polymerase. Radiolabeled precursor proteins were synthesized in a cell-free translation system using reticulocyte lysate in the presence of ³⁵S-methionine and ³⁵S-cysteine (EXPRE³⁵S Protein Labeling Mix, [³⁵S]-, PerkinElmer). Isolated mitochondria (25–100 μ g protein) were incubated with radiolabeled proteins in import buffer (pH 7.2, 10 mM MOPS-KOH, 2.5 mM KH₂PO₄-K₂HPO₄, 250 mM sucrose, 80 mM KCl, 5 mM MgCl₂, 2 mM ATP, 2 mM methionine, 2 mM NADH, 5 mM DTT, 12 mM creatine phosphate, 0.12 mg/mL creatine phosphokinase, 1% (w/v) BSA) at 25 °C for indicated periods. Import reactions were stopped by adding valinomycin (10 μ g/mL) for $\Delta\Psi$ dependent import, iodoacetamide (50 mM) for small TIM protein import, or 4-fold dilution with SEM buffer (250 mM sucrose, 10 mM MOPS-KOH, pH 7.2, 1 mM EDTA) for other precursor protein import, followed by shifting the reaction tubes onto ice. Precursor proteins outside the mitochondria were digested with 50 μ g/mL proteinase K on ice for 20 min, and the reaction was stopped by adding PMSF to a final concentration of 1 mM. Mitochondria were re-isolated by centrifugation at 13,000 \times g for 5 min at 4 °C, and washed with SEM buffer (250 mM sucrose, 10 mM MOPS-KOH, pH 7.2, 1 mM EDTA, 1 mM PMSF). Proteins were analyzed by SDS-PAGE or BN-PAGE, followed by radio-imaging using an Imaging Plate and a Typhoon FLA-7000 image analyzer (GE Healthcare).

The M2M crosslinking assay (Fig. 1e) was performed as described⁶¹. Briefly, the *por1* Δ strain was transformed with a plasmid encoding a Por1 double-Cys mutant. After cultivation in 20 mL of SCD (-Trp) for 24 h at 30 °C, the culture was incubated at 30 °C, and cells were harvested by centrifugation (1500 \times g, 5 min, 4 °C). Mitochondria were isolated using the procedure described above and treated with 1 mM M2M (1,2-ethanedithiol bismethanethiosulfonate) for 10 min. Free SH groups were then blocked with 50 mM iodoacetamide for 10 min.

In vivo BPA photocrosslinking²¹ (Fig. 2d) was performed as follows. Briefly, culturing conditions (in the dark) are as follows. For overexpression of Tom22 with the C-terminally attached His₁₀ tag (Tom22-His10) containing BPA, *por1* Δ strain constitutively expressing Z4EV (transcription factor induced by β -estradiol) was transformed with the plasmids, p6xtRNA, pRS316/Por1-HA or Por1(KE)-HA and pRS315/Z4EVp-Tom22 L118amb (Supplementary Table 2), which were then grown in SD (-Trp, -Leu, -Ura, + 1 mM BPA, and 1 mM β -estradiol) for 16–24 h at 30 °C. The cultured yeast cells were harvested and divided into halves. One half was UV-irradiated for 10 min at room temperature at a distance of 5 cm from a 365 nm UV lamp with a power of 22,000 mW/cm² (B-100AP; UVP, Upland, CA, USA), and the other half was kept on ice in the dark. The yeast cell pellets were stored at -20 °C until use. His-tagged BPA-containing Tom22 and its cross-linked products were affinity-purified with Ni-NTA agarose²¹.

Crosslinked partner proteins were identified by immunoblotting with antibodies against Tom22 or HA (Por1).

Mitochondrial permeability assay

The mitochondrial permeability assay⁶² was performed as follows. To assess permeability via Por1, NADH oxidation in the IMS by Nde1/2 in the IM was measured by monitoring the decrease in the absorbance at 340 nm. Purified mitochondria containing Por1 mutants, suspended in SEM buffer, were used as samples. The oxidation reaction was initiated by adding NADH to a final concentration of 60 μM to 60 $\mu\text{g}/\text{mL}$ of mitochondria. Absorbance was measured at intervals of 1–2 min over an 8 min period.

Phospholipid analysis

Yeast cells were diluted to an OD₆₀₀ of 0.02 in 1 mL of YPD medium containing 5 mCi/mL [³²P]-Pi and cultured at 30 °C for 16 h. The cells were collected by centrifugation and vortexed for 20 min in 330 μL methanol with 100 μL glass beads. Subsequently, 600 μL of chloroform was added, mixed, and centrifuged at 12,000 rpm for 10 min. The supernatant was transferred to a new tube containing 200 μL of 0.1 M HCl and 0.5 M NaCl, vortexed for 5 min, and centrifuged at 2000 $\times g$ for 5 min. The organic layer was collected and dried under nitrogen gas. The dried lipids were dissolved in 60 μL of chloroform, with 20 μL subjected to TLC analysis using a chloroform/ethanol/water/triethylamine (30:35:7:35) solvent system. Radiolabeled phospholipids were analyzed by radioimaging using a Typhoon scanner (Cytiva).

Coarse-grained molecular dynamics (CGMD) simulation

System preparation and settings; the initial structure of the Por1 hexamer was based on our cryo-EM structure. First, the atomistic structure was minimized in a vacuum using the AMBER99SB-ILDN force field⁶³ and the steepest descent method, with a maximum force tolerance of 100 $\text{kJmol}^{-1}\text{nm}^{-1}$ per atom. Coarse-graining of the minimized structure for the Martini 3.0 force field⁶⁴ was performed using the Martinize2 script⁶⁵. The coarse-grained (CG) structure was then embedded in a hydrated 1-palmitoyl-2-oleoyl-sn-glycero-3-phosphocholine (POPC) bilayer containing 100 mM NaCl, using the INSANE script^{66,67}. The size of the simulation box or single cell was 20 \times 20 \times 12 nm. The CG system was further minimized using the Martini 3.0 force field, with a maximum force tolerance of 200 $\text{kJ mol}^{-1} \text{nm}^{-1}$. In addition to the Por1 hexamer, coarse-grained molecular dynamics (CGMD) simulations were conducted for the Por1 monomer, Por1 dimer, and a pure hydrated bilayer system. Chain A of the hexamer structure was adopted as the initial model of the monomer, while three distinct chain pairs from the hexamer (referred to as dimer AB', dimer AC, and dimer BC, based on chain IDs) were used for the dimers. The preparation and settings for these systems were identical to those of the hexamer, with cell sizes of 18 \times 18 \times 12 nm for the dimers and 15 \times 15 \times 12 nm for the monomer. Previous all-atom MD simulations of mouse VDAC1 showed that single point mutations can affect dynamics in the N-terminal barrel and membrane thinning²⁷. Based on this, additional simulations were performed for two Por1 mutants, Q73E and Q73V. Simulations included the Q73E and Q73V hexamers, dimer AB', dimer AC, dimer BC, and a Q73E monomer. The system compositions, namely the number of molecules for CGMD simulations, are listed in Supplementary Table 5. The initial structures for the mutant oligomers and monomers were derived from the cryo-EM structures, with side chain conformations for the mutants prepared using SCWRL4.0 software⁶⁸.

Equilibration and production simulation protocol; a five-step equilibration protocol was employed, progressively increasing time step width (dt) and simulation duration (t): 1) $dt = 2$ fs, $t = 0.5$ ns, 2) $dt = 10$ fs, $t = 1.25$ ns, 3) $dt = 20$ fs, $t = 30$ ns, 4) $dt = 20$ fs, $t = 15$ ns, 5) $dt = 20$ fs, $t = 10$ ns²⁴. For all stages, the temperature was maintained at 300 K using the velocity-rescaling method, and

the pressure was maintained at 1.0 bar using the Berendsen barostat. Three independent 20 μs (100 μs for hexamer (WT)) production runs were performed for each system, using the same settings as in the fifth equilibration stage, except that the Parrinello-Rahman barostat was used instead of the Berendsen barostat. For the control system of a pure hydrated bilayer, one 10 μs production run was performed. During simulations, residues near the phosphorus atom of the phospholipid head group were counted and normalized by the total number of scrambles occurring near the interface. The residues with a rate larger than 0.6 were defined as frequently involved residues in the scrambling process. All CGMD simulations and energy minimizations were performed using GROMACS (version 2023.0)⁶⁹.

Quantification of mitochondrial DNA

Yeast cells (1.0×10^7 cells) were washed with 50 mM Tris-HCl, pH 8.0, 100 mM NaCl. Total yeast DNA was isolated using the Phenol-chloroform extraction method. Briefly, yeast pellets were resuspended in 200 μL of genome prep buffer (10 mM Tris-HCl, pH 8.0, 100 mM NaCl, 1 mM EDTA, 2% TritonX-100, 1% SDS), 200 μL of PCI (phenol/chloroform/isoamyl alcohol, 25:24:1), and 0.6 mm zirconia/silica beads. The mixture was vigorously stirred for 2 min at room temperature, followed by centrifugation at 16,000 $\times g$ for 1 min. The supernatant was transferred to a new tube and mixed with 200 μL of PCI, followed by another centrifugation at 16,000 $\times g$ for 1 min. The supernatant was transferred to a new tube and centrifuged at 16,000 $\times g$ for 1 min. Finally, the supernatant was collected and diluted 1:10 with water. Quantitative PCR (qPCR) was performed using TB Green Premix ExTaq II (RR820; TaKaRa) and the primers listed in Supplementary Table 3, on the Mic real-time PCR cycler (Bio Molecular Systems). Data were analyzed by the 2^{- $\Delta\Delta\text{CT}$} method, with normalization to the *ACT1* gene. The quality of the qPCR results was evaluated based on the melting temperature (T_m) of the DNA fragments and melting curve analysis. For the time course analysis of mtDNA depletion, yeast strains were grown in SCD (-Trp) medium at 30 °C until they reached stationary phase. Subsequently, 0.2 OD₆₀₀ units of cells were transferred to SCGal (-Trp) medium to induce expression of either Por1(WT) or Por1(Q194A). One OD₆₀₀ unit of cells were collected periodically and stored at -80 °C until use.

Fluorescent microscopy

For localization of mtDNA, yeast cells expressing Por1(WT) or Por1(Q194A) from their own promoter were grown in SCD (-Trp, 2 \times Ade) medium containing with SYBR Green I (1:4000, S7563; Thermo Fisher Scientific) for 4 h at 30 °C. For localization of Abf2, yeast cells expressing Abf2-mNeonGreen from its own promoter, along with Por1(WT) or Por1(Q194A), were cultured in SCD (-Trp and 2 \times Ade) medium for 4 h at 30 °C. For localization of MDL proteins, yeast cells expressing MDL proteins tagged with mNeonGreen from either its own promoter or the *GPD* promoter were grown in YPD or SCD (-Ura, 2 \times Ade) medium for 4 h at 30 °C. Cells were mounted on 1.5% gellan gum (073-03071; Fujifilm Wako Pure Chemical Corporation) on glass coverslips (Matsunami glass). Imaging was performed using a confocal microscope (AI; Nikon) equipped with a 100 \times Apo TIRF oil-immersion objective lens (Nikon, NA 1.49) or a spinning-disk super resolution microscopy (IXplore SpinSR spinning-disk super resolution microscope system; Evident) using a 60 \times oil-immersion objective lens (PlanApo N 60 \times /1.40 Oil SC; Evident). Z-series images were captured at every 0.2 μm from the top to the bottom surface of the yeast cells. Super-resolution images were deconvolved with Huygens Professional Software Suite (version 21.04, Scientific Volume Imaging B.V., Hilversum, The Netherlands) using the Spinning Disk deconvolution option software optimized for Nipkow disk based spinning disk microscopy. Image processing and analysis were conducted using Fiji ImageJ software⁷⁰.

To test the mitochondrial localization of the MDL proteins using the Bi-Genomic Mitochondrial-Split-GFP strain, the RKY176 yeast strain, transformed with the indicated plasmid, was grown at 30 °C in SCGal (-Trp) medium. Exponential growing yeast cells were observed by high-resolution microscopy⁷¹, using a confocal microscope (LSM 800; Zeiss) equipped with a highly sensitive Airyscan detector (32-channel gallium arsenide phosphide photomultiplier tube). Images were acquired using the Zeiss Zen Blue software with a laser residence time per pixel (pixel dwell time) of 11.8 μs.

Statistics and Reproducibility

All experiments in this study have been reproduced using the same experimental set-up (cell extracts, mitochondrial proteins, buffers, detergents, affinity matrices, etc., independent biological experiments) with similar results. For SDS-PAGE, Western blots, radio-imaging, and microscopy, representative results from two or more independent experiments are shown. Replications confirming all presented data are available. For sample sizes, the amount of mitochondrial and cellular proteins used for the biochemical assays was chosen based on previous experiences with this specific type of experiment and commonly used sample sizes in the field of research. For key experiments, several test runs were performed to determine the optimal sample size used.

Reporting summary

Further information on research design is available in the Nature Portfolio Reporting Summary linked to this article.

Data availability

The cryo-EM density map has been deposited in the Electron Microscopy Data Bank under accession code 61843 [<https://www.ebi.ac.uk/emdb/api/yearly/9JVQ>]. The atomic coordinates have been deposited in the Protein Data Bank under accession code 9JVQ. All other data are included in the manuscript and/or supporting information. Source data are provided in this paper.

Code availability

Input files used for the molecular dynamics simulations are available via FigShare under the <https://doi.org/10.6084/m9.figshare.28665635>.

References

- Blachely-Dyson, E., Peng, S., Colombini, M. & Forte, M. Selectivity changes in site-directed mutants of the VDAC ion channel: structural implications. *Science* **247**, 1233–1236 (1990).
- Shoshan-Barmatz, V., Krelan, Y. & Shteinifer-Kuzmine, A. VDAC functions in Ca²⁺ homeostasis and cell life and death in health and disease. *Cell Calcium* **69**, 81–100 (2018).
- Zhou, R., Yazdi, A. S., Menu, P. & Tschopp, J. A role for mitochondria in NLRP3 inflammasome activation. *Nature* **469**, 221–225 (2011).
- Cheng, E. H., Sheiko, T. V., Fisher, J. K., Craigen, W. J. & Korsmeyer, S. J. VDAC2 inhibits BAK activation and mitochondrial apoptosis. *Science* **301**, 513–517 (2003).
- Colombini, M. et al. VDAC structure, selectivity, and dynamics. *Biochim. Biophys. Acta* **1818**, 1457–1465 (2012).
- Hiller, S. et al. Solution structure of the integral human membrane protein VDAC-1 in detergent micelles. *Science* **321**, 1206–1210 (2008).
- Ujwal, R. et al. The crystal structure of mouse VDAC1 at 2.3Å resolution reveals mechanistic insights into metabolite gating. *Proc. Natl. Acad. Sci. USA* **105**, 17742–17747 (2008).
- Bayrhuber, M. et al. Structure of the human voltage-dependent anion channel. *Proc. Natl. Acad. Sci. USA* **105**, 15370–15375 (2008).
- Schredelseker, J. et al. High resolution structure and double electron-electron resonance of the zebrafish voltage-dependent anion channel 2 reveal an oligomeric population. *J. Biol. Chem.* **298**, 12566–12577 (2014).
- Choudhary, O. P. et al. Structure-guided simulations illuminate the mechanism of ATP transport through VDAC1. *Nat. Struct. Mol. Biol.* **21**, 626–634 (2014).
- Böhm, R. et al. The structural basis for low conductance in the membrane protein VDAC upon β-NADH binding and voltage gating. *Structure* **28**, 206–214 (2019).
- Hosaka, T. et al. Crystal structural characterization reveals novel oligomeric interactions of human voltage-dependent anion channel 1. *Protein Sci.* **26**, 1749–1758 (2017).
- Kozjak-Pavlovic, V. et al. Conserved roles of Sam50 and metaxins in VDAC biogenesis. *EMBO Rep.* **8**, 576–582 (2007).
- Callegari, S. et al. Structure of human PINK1 at a mitochondrial TOM-VDAC array. *Science* **388**, 303–310 (2025).
- Mannella, C. A. et al. Structure of the mitochondrial outer membrane channel derived from electron microscopy of 2D crystals. *J. Bioenerg. Biomembr.* **21**, 427–437 (1989).
- Guo, X. W., Smith, P. R. & Mannella, C. A. Molecular design of the voltage-dependent anion-selective channel in the mitochondrial outer membrane. *J. Struct. Biol.* **114**, 41–59 (1995).
- Goncalves, R. P. et al. Supramolecular assembly of VDAC in native mitochondrial outer membranes. *J. Mol. Biol.* **369**, 413–418 (2007).
- Hoogenboom, B. W. et al. The supramolecular assemblies of voltage-dependent anion channels in the native membrane. *J. Mol. Biol.* **370**, 246–255 (2007).
- Hiller, S. et al. The 3D structures of VDAC represent a native conformation. *Trends Biochem. Sci.* **35**, 514–521 (2010).
- Zeth, K. et al. Ten years of high-resolution structural research on the voltage dependent anion channel (VDAC) – recent developments and future directions. *Front. Physiol.* **9**, <https://doi.org/10.3389/fphys.2018.00108> (2018).
- Sakaue, H. et al. Porin associates with Tom22 to regulate the mitochondrial protein gate assembly. *Mol. Cell* **73**, 1044–1055 (2019).
- Gornicka, A. et al. A discrete pathway for the transfer of inter-membrane space proteins across the outer membrane of mitochondria. *Mol. Biol. Cell* **25**, 3999–4009 (2014).
- Tatsuta, T. et al. Intramitochondrial phospholipid trafficking. *Biochim. Biophys. Acta* **1862**, 81–89 (2017).
- Tamura, Y., Kawano, S. & Endo, T. Lipid homeostasis in mitochondria. *Biol. Chem.* **401**, 821–833 (2020).
- Jahn, H. et al. Phospholipids are imported into mitochondria by VDAC, a dimeric beta barrel scramblase. *Nat. Commun.* **14**, 8115 (2023).
- Li, D., Rocha-Roa, C., Schilling, M. A., Reinisch, K. M. & Vanni, S. Lipid scrambling is a general feature of protein insertase. *Proc. Natl. Acad. Sci. USA* **121**, e2319476121 (2023).
- Villinger, S. et al. Functional dynamics in the voltage-dependent anion channel. *Proc. Natl. Acad. Sci. USA* **107**, 22546–22551 (2010).
- Pollack, Y., Kasir, J., Shemer, R., Metzger, S. & Szyf, M. Methylation pattern of mouse mitochondrial DNA. *Nucleic Acids Res.* **12**, 4811–4824 (1984).
- Cardon, L., Burge, C., Clayton, D. A. & Karlin, S. Pervasive CpG suppression in animal mitochondrial genomes. *Proc. Natl. Acad. Sci. USA* **91**, 3799–3803 (1994).
- Gray, M. W., Burger, G. & Lang, B. F. Mitochondrial evolution. *Science* **283**, 1476–1481 (1999).
- Taanman, J. W. et al. The mitochondrial genome: structure, transcription, translation and replication. *Biochim. Biophys. Acta* **1410**, 103–123 (1999).
- Collins, L., Hajizadeh, S., Holme, E., Jonsso, K. & Tarkowski, A. Endogenously oxidized mitochondrial DNA induces in vivo and in vitro inflammatory responses. *J. Leukoc. Biol.* **75**, 995–1000 (2004).

33. Kim, J., Kim, H. S. & Chung, J. H. Molecular mechanisms of mitochondrial DNA release and activation of the cGAS-STING pathway. *Exp. Mol. Med.* **55**, 510–519 (2023).
34. Bahat, A., MacVicar, T. & Langer, T. Metabolism and innate immunity meet at the mitochondria. *Front. Cell Dev. Biol.* **9**, 720490 (2021).
35. Zhou, W. et al. Somatic nuclear mitochondrial DNA insertions are prevalent in the human brain and accumulate over time in fibroblasts. *PLoS Biol.* **22**, e3002723 (2024).
36. Cheng, X. & Ivessa, A. S. The migration of mitochondrial DNA fragments to the nucleus affects the chronological aging process of *Saccharomyces cerevisiae*. *Aging Cell* **9**, 919–923 (2010).
37. Kim, J. et al. VDAC oligomers form mitochondrial pores to release mtDNA fragments and promote lupus-like disease. *Science* **366**, 1531–1536 (2019).
38. Galeota-Sprung, B., Fernandez, A. & Sniegowski, P. Changes to the mtDNA copy number during yeast culture growth. *R. Soc. Open Sci.* **9**, 211842 (2022).
39. Mizushima, N., Levine, B., Cuervo, A. M. & Klionsky, D. J. Autophagy fights disease through cellular self-digestion. *Nature* **451**, 1069–1075 (2008).
40. Newman, L. E. et al. Mitochondrial DNA replication stress triggers a pro-inflammatory endosomal pathway of nucleoid disposal. *Nat. Cell Biol.* **26**, 194–206 (2024).
41. Liu, H. et al. TFAM is an autophagy receptor that limits inflammation by binding to cytoplasmic mitochondrial DNA. *Nat. Cell Biol.* **26**, 878–891 (2024).
42. Sharma, N. & Osman, C. Yme2, a putative RNA recognition motif and AAA+ domain containing protein, genetically interacts with the mitochondrial protein export machinery. *Biol. Chem.* **403**, 807–817 (2022).
43. Casari, E. et al. Processing of DNA double-strand breaks by the MRX complex in a chromatin context. *Front. Mol. Biosci.* **6**, 43 (2019).
44. Bader, G. et al. Assigning mitochondrial localization of dual localized proteins using a yeast Bi-Genomic Mitochondria-Split-GFP. *ELife* **9**, e56649 (2020).
45. Hanekamp, T. & Thorsness, P. E. YNT20, a bypass suppressor of *yme1*, *yme2*, encodes a putative 3'-5' exonuclease localized in mitochondria of *Saccharomyces cerevisiae*. *Curr. Genet.* **34**, 438–448 (1999).
46. Park, S., Hanekamp, T., Thorsness, M. K. & Thorsness, P. E. Yme2p is a mediator of nucleoid structure and number in mitochondria of the yeast *Saccharomyces cerevisiae*. *Curr. Genet.* **50**, 173–182 (2006).
47. Murley, A. et al. ER-associated mitochondrial division links the distribution of mitochondria and mitochondrial DNA in yeast. *ELife* **2**, e00422 (2013).
48. Bykov, S. Y. et al. A systematic bi-genomic split-GFP assay illuminates the mitochondrial matrix proteome and protein targeting routes. *ELife* **13**, RP98889 (2024).
49. Longtine, M. S. et al. Additional modules for versatile and economical PCR-based gene deletion and modification in *Saccharomyces cerevisiae*. *Yeast* **14**, 953–961 (1998).
50. Zivanov, J. et al. New tools for automated high-resolution cryo-EM structure determination in RELION-3. *ELife* **7**, e42166 (2018).
51. Rohou, A. & Grigorieff, N. CTFIND4: Fast and accurate defocus estimation from electron micrographs. *J. Struct. Biol.* **192**, 216–221 (2015).
52. Rosenthal, P. B. & Henderson, R. Optimal determination of particle orientation, absolute hand, and contrast loss in single-particle electron cryomicroscopy. *J. Mol. Biol.* **333**, 721–745 (2003).
53. Pettersen, E. F. et al. UCSF Chimera – a visualization system for exploratory research and analysis. *J. Comput. Chem.* **25**, 1605–1612 (2004).
54. Emsley, P., Lohkamp, B., Scott, W. G. & Cowtan, K. Features and development of Coot. *Acta Crystallogr. D Biol. Crystallogr.* **66**, 486–501 (2010).
55. Terwilliger, C. T. et al. New tools for the analysis and validation of cryo-EM maps and atomic models. *Acta Crystallogr. Sect. D Struct. Biol.* **74**, 814–840 (2018).
56. Ishitani, R. CueMol. available at <http://www.cuemol.org>.
57. Ando, T. et al. A high-speed atomic force microscope for studying biological macromolecules. *Proc. Natl. Acad. Sci. USA* **98**, 12468–12472 (2001).
58. Ando, T., Uchihashi, T. & Fukuma, T. High-speed atomic force microscopy for nano-visualization of dynamic biomolecular processes. *Prog. Surf. Sci.* **83**, 337–437 (2008).
59. Uchihashi, T., Kodera, N. & Ando, T. Guide to video recording of structure dynamics and dynamic processes of proteins by high-speed atomic force microscopy. *Nat. Protoc.* **7**, 1193–1206 (2012).
60. Amyot, R. & Flechsig, H. BioAFMviewer: An interactive interface for simulated AFM scanning of biomolecular structures and dynamics. *PLoS Comput. Biol.* **16**, e1008444 (2020).
61. Guan, Z. et al. Structural insight into assembly of human mitochondrial translocase TOM complex. *Cell. Discov.* **7**, 22 (2021).
62. Ellnrieder, L. et al. Dual role of mitochondrial porin in metabolite transport across the outer membrane and protein transfer to the inner membrane. *Mol. Cell.* **73**, 1056–1065 (2019).
63. Lindorff-Larsen, K. et al. Improved side-chain torsion potentials for the Amber ff99SB protein force field. *Proteins Struct. Funct. Bioinform.* **78**, 1950–1958 (2010).
64. Souza, P. C. T. et al. Martini 3: a general purpose force field for coarse-grained molecular dynamics. *Nat. Methods* **18**, 382–388 (2021).
65. Kroon, P. C. et al. Martinize2 and vermouth: Unified framework for topology generation. *Elife* <https://doi.org/10.7554/eLife.90627.3> (2023).
66. Wassenaar, T. A. et al. Computational lipidomics with insane: A versatile tool for generating custom membranes for molecular simulations. *J. Chem. Theory Comput.* **11**, 2144–2155 (2015).
67. GitHub - Tsjerk/Insane: INSert membrANE - A simple, versatile tool for building coarse-grained simulation systems, (available at <https://github.com/Tsjerk/Insane>) (2024).
68. Wang, Q., Canutescu, A. A. & Dunbrack, R. L. SCWRL and MolIDE: computer programs for side-chain conformation prediction and homology modeling. *Nat. Protoc.* **3**, 1832–1847 (2008).
69. Abraham, M. J. et al. GROMACS: High performance molecular simulations through multi-level parallelism from laptops to supercomputers. *SoftwareX.* **1–2**, 19–25 (2015).
70. Rasband, W. S. et al. ImageJ, U.S. National Institutes of Health. available at <http://imagej.nih.gov/ij/> (2018).
71. Zutton, S. et al. Monitoring mitochondrial localization of dual localized proteins using a Bi-Genomic Mitochondrial-Split GFP. *Methods Enzymol.* **706**, 75–95 (2024).

Acknowledgements

We thank the members of the T.E. lab for the discussion and critical comments on the manuscript. Technical assistance by Kyoko Nakamura (Endo lab) is acknowledged. We also thank Yasushi Okada and Sawako Enoki (University of Tokyo) for fluorescence microscopy measurements. HS-AFM measurements were supported by the Bio-SPM collaborative research program to Y.A., Kanazawa University. This work was supported by JSPS KAKENHI to T.E. (15H05705 and 2222703), H.T. (18K14640), and S.S. (22K15108, 24K02026).; JST CREST grant to T.E. (JPMJCR12M1) and AMED CREST grant to T.E. (21gm1410002h0002). The following grants are also acknowledged; a grant from Takeda Science Foundation (to T.E.), Platform Project for Supporting Drug Discovery and Life Science Research (Basis for Supporting Innovative Drug Discovery and Life Science Research (BINDS)) from AMED under grant numbers JP24ama121002 (to M.K.), JP24ama121028 (support number 4633) (to K.T.), and JST FOREST program grant (JPMJFR230Y) to H.T. H.T. (18J00358), H.S. (20J00033), T.H. (23KJ2067), and S.S. (19J00899) were

supported by a Research Fellowship for Young Scientists from the Japan Society of the Promotion of Science. H.D.B. and S.F. laboratories were supported by funding from the Center National de la Recherche Scientifique (CNRS), Université de Strasbourg (France), and IdEx Unistra (ANR-10-IDEX-0002). H.D.B. and S.Z. are also supported by the Integrative Molecular and Cellular Biology (IMCBio) EUR (ANR-17-EURE-0023) under the framework of the French Investments for the Future Program, as part of the Interdisciplinary Thematic Institutes (ITI) 2021–2028 program of the University of Strasbourg, CNRS, and INSERM.

Author contributions

Conceptualization and writing: T.E., H.T. and S.S.; Lipid analyses: Hi.S. and Y.T.; Import and assembly assays: Ha.S. and Y.K.; Gel electrophoresis and Western blotting: H.T., Ha.S. and T.H.; Yeast growth assays: H.T., Ha.S. and T.H.; qPCR: C.G., H.O. and S.S.; Microscopy: S.Z., B.S., S.F., H.D.B., H.O. and S.S.; DNA constructions: H.T., Ha.S., T.H., H.O., C.G., Y.K. and S.S.; Mitochondrial permeability assays: H.T.; Protein purification: H.T., C.G. and C.Z.; Cryo-EM measurements, data processing, and model building: H.T., A.T., C.G., C.Z. and M.K.; MD simulation: K.T. and Y.Y.; HS-AFM measurements and data processing: H.T., S.S., C.G., C.Z., Y.A., Na.K. and No.K.

Competing interests

The authors declare no competing interests.

Additional information

Supplementary information The online version contains supplementary material available at <https://doi.org/10.1038/s41467-025-62021-4>.

Correspondence and requests for materials should be addressed to Toshiya Endo.

Peer review information *Nature Communications* thanks Anant Menon, Kostas Tokatlidis, Stefano Vanni, Matthias Wolf, and the other anonymous reviewer(s) for their contribution to the peer review of this work. A peer review file is available.

Reprints and permissions information is available at <http://www.nature.com/reprints>

Publisher's note Springer Nature remains neutral with regard to jurisdictional claims in published maps and institutional affiliations.

Open Access This article is licensed under a Creative Commons Attribution-NonCommercial-NoDerivatives 4.0 International License, which permits any non-commercial use, sharing, distribution and reproduction in any medium or format, as long as you give appropriate credit to the original author(s) and the source, provide a link to the Creative Commons licence, and indicate if you modified the licensed material. You do not have permission under this licence to share adapted material derived from this article or parts of it. The images or other third party material in this article are included in the article's Creative Commons licence, unless indicated otherwise in a credit line to the material. If material is not included in the article's Creative Commons licence and your intended use is not permitted by statutory regulation or exceeds the permitted use, you will need to obtain permission directly from the copyright holder. To view a copy of this licence, visit <http://creativecommons.org/licenses/by-nc-nd/4.0/>.

© The Author(s) 2025